This article has been accepted for publication in IEEE Transactions on Geoscience and Remote Sensing. This is the author's version which has not been fully edited and content may change prior to final publication. Citation information: DOI 10.1109/TGRS.2024.3369509

A Generalized Beta Prime Distribution as the Ratio Probability Density Function for Change Detection Between two SAR Intensity Images with Different Number of Looks

Gerard Gallardo i Peres, Jørgen Dall, *Member, IEEE*, Philippa J Mason, Richard Ghail, and Scott Hensley, *Fellow, IEEE*

***Abstract*—In the framework of the comparison of Synthetic Aperture Radar (SAR) imagery from the Magellan space mission and the VISAR and VenSAR radar instruments which will be onboard the forthcoming VERITAS and EnVision missions to Venus, the problem of the disparity between the resolutions of the images arises when attempting to define a test statistic with which to detect changes. Reliable change detection requires equivalent spatial resolutions which, for the two different images, inevitably involves different equivalent number of looks after speckle-reduction processing. This study presents a method to address this scenario using a Generalized Beta Prime Distribution as a probability density function (*PDF*) which is fit to the histogram of the ratio between the two intensity images. The work demonstrates and verifies the properties of the function, highlights its most useful traits, and elaborates on the mathematical procedure required to achieve a meaningful change detection in line with the classic theory of equal number of looks. The results show that the method accurately describes the ratio histogram of two SAR intensity images with different number of looks. Furthermore, they demonstrate the adaptability of the method to the presence of high pixel correlation between the images, and validate its robustness in the presence of textural complexity when the texture patterns of the images are similar.**

***Index Terms*—Change detection, resolution, probability distribution, SAR, Venus.**

Manuscript received September 8, 2023; revised Month XX, XXXX. This work was supported by an ESA OSIP grant and isardSAT S.L.

Gerard Gallardo i Peres is with Imperial College London, London, SW7 2AZ, United Kingdom, and isardSAT S.L., Barcelona, 08042, Spain (e-mail: g.g.peres@imperial.ac.uk).

Jørgen Dall is with the Technical University of Denmark, Kgs. Lyngby, 2800, Denmark (e-mail: jdall@dtu.dk).

Philippa J Mason is with Imperial College London, London, SW7 2AZ, United Kingdom (e-mail: p.j.mason@imperial.ac.uk).

Richard Ghail is with the Royal Holloway, University of London, Egham, TW20 0EX, United Kingdom (e-mail: Richard.Ghail@rhul.ac.uk).

Scott Hensley is with the Jet Propulsion Laboratory, Pasadena, Ca 91109, USA (e-mail: shensley@jpl.nasa.gov).

I. Introduction

CHANGE detection comprises a powerful family of techniques that is applied to a variety of remotely sensed datasets and applications to monitor the surface processes of the Earth and other planets. Considering airborne or spaceborne Synthetic Aperture Radar (SAR) instruments, multiple observations of the same target area can lead to the identification of surface changes occurring in the time interval between the measurements. The inherent coherence of SAR imagery can be exploited by techniques such as Differential Interferometric SAR (DInSAR) [1] or coherent change detection (CCD) [2] to map surface changes between observations with great accuracy. DInSAR makes use of the change-related component of the interferometric phase to obtain the magnitude and direction of displacements with millimetre accuracy on Earth [3], and it is often utilized in the monitoring and impact assessment of events such as earthquakes [4], landslides [5] and ice flow [6].

Localized loss of coherence between SAR observations has also been used successfully to detect new lava flow emplacements in volcanic eruptions [7], [8], and other changes. However, these techniques cannot be applied where complete decorrelation occurs, which may happen for a variety of reasons: the rate of change is too great compared to the temporal baseline of the observations; inaccuracies in the image co-registration process; the viewing geometry of the two observations is not compatible for interferometry; or simply because the SAR images come from different sensors, with different carrier frequencies or polarizations.

Authorized licensed use limited to: Imperial College London. Downloaded on March 01,2024 at 10:36:50 UTC from IEEE Xplore. Restrictions apply.
© 2024 IEEE. Personal use is permitted, but republication/redistribution requires IEEE permission. See https://www.ieee.org/publications/rights/index.html for more information.

This article has been accepted for publication in IEEE Transactions on Geoscience and Remote Sensing. This is the author's version which has not been fully edited and content may change prior to final publication. Citation information: DOI 10.1109/TGRS.2024.3369509

In these scenarios, the phase of SAR imagery does not encode change information, and the detection of changes can only exploit the information present in the intensity or magnitude, usually given in the σ_0 backscatter form. So-called incoherent change detection techniques have been generally applied to SAR intensity images before coherent techniques were available, and in the cases where coherent change detection is not possible; these techniques usually rely on methods of offset-tracking [9] or otherwise on test statistics [2]. Offset - or feature - tracking provides estimates of the magnitude and direction of changes by optimizing intensity cross-correlation of image patches, and it has been applied to glacier [10], land mass [11] and dune [12] displacements. Although robust, it does not achieve the change detection accuracy provided by coherent techniques, and it moreover requires feature preservation between images, which makes its application difficult when monitoring disruptive events such as explosive volcanism, or dynamic processes such as lava flow emplacements.

On the other hand, test statistics, understood as the statistical test of a hypothesis of similarity between observed data and a known model or mathematical distribution, have been employed as a tool for SAR change detection analysis in a multitude of studies. These include single-channel unsupervised approaches [13]–[15], supervised and semi-supervised methods based on different Machine Learning techniques [16]–[18], changes found in polarimetric sequences of SAR imagery [19]–[21], and recent generalization efforts on a common change detection framework [22] for different types of imagery. A good summary of the most used SAR change detection techniques based on test statistics can be found in [23], [24].

One of its most basic uses is the likelihood-ratio test statistic, which uses two co-registered SAR images and fits a probability density function to the histogram of the ratio image, then identifies the pixels that fall outside the predicted behaviour. This technique is able to map, and classify as change or no-change, any pixel-level changes in SAR images without the need of coherence or feature preservation; it is able to identify areas that have changed to a certain statistical confidence, although it cannot infer displacement magnitudes and directions. It is this particular technique that is the basis for the approach developed here.

The statistical modelling of SAR intensity imagery in different forms and of diverse clutter types has been a widely approached problem since the early 1980s. There are several important studies which built on the initial forms of Gamma distributions to model homogeneous terrain [25] and on $\mathcal{K}$ distributions to model textured, distributed targets [26]; the generalized inverse Gaussian distribution framework was proposed in [27] to model a vast array of clutter types. A number of statistical distributions stemming from the more general family of $\mathcal{G}$ distributions have been used to model SAR clutter [28], for classification problems with Gaussian maximum likelihood [29], in problems of SAR edge detection [30], and in the field of polarimetric target detection [31]. In this study, a particular distribution named the 'generalized Beta prime distribution' is introduced and described in the context of SAR ratio test statistics. It is then developed as a general case of the classical theory of single-channel ratio test statistics that can deal with images with very different spatial resolutions, providing a simple but malleable analytical framework that can work with different types of clutter. This opens the door to tackling change detection problems using data from different SAR sensors, acquired at different times.

In the context of exploring the surface of the planet Venus, the most recent SAR data available is from the Magellan mission, acquired in the early 1990s [32]. Several new planetary missions, including EnVision [33] and VERITAS [34], will be launched in the following decade, targeting Venus with new, upgraded SAR sensors. They are estimated to have 90 % chance of detecting post-Magellan volcanic activity, even if it is at the lowest end of prediction, by imaging only 10 % of the surface and comparing those observations with Magellan data [35]. It is estimated that at least 120 discrete eruptions may occur on Venus per Earth year [36], while other surface changes due to tectonic, aeolian or weathering processes are also expected in the 40-year temporal baseline between the missions [37]. Since the planned spatial resolution of the new sensors is around an order of magnitude better than Magellan [38], the ability to reliably detect changes on Venus within this time period decisively depends, among other factors, on an improved SAR test statistic framework that can effectively deal with data of greatly differing spatial resolutions.

A reliable, automated intermission SAR change detection procedure, between Magellan and VERITAS or EnVision, is therefore an important objective and a necessity for a successful future Venus exploration. Moreover, this procedure also has the potential to be broadened and developed for Earth observation purposes, where there is a much larger and more diverse range of SAR systems available. This study presents an approach

Authorized licensed use limited to: Imperial College London. Downloaded on March 01,2024 at 10:36:50 UTC from IEEE Xplore. Restrictions apply.
© 2024 IEEE. Personal use is permitted, but republication/redistribution requires IEEE permission. See https://www.ieee.org/publications/rights/index.html for more information.

This article has been accepted for publication in IEEE Transactions on Geoscience and Remote Sensing. This is the author's version which has not been fully edited and content may change prior to final publication. Citation information: DOI 10.1109/TGRS.2024.3369509

to deal with one of the major challenges of intermission change detection: that of a large difference in spatial resolution. Other challenges include differences in the SAR carrier frequency, polarization, and thermal noise levels, all of which play a central role in the definition of the SAR signal and its interaction with its target. All these factors distort the retrieved SAR intensity images; a way to make the two datasets comparable must therefore be devised before effective and robust change detection can be achieved.

This paper is organised as follows. Section II describes the ratio change statistic as applied to a classic case. The problem that arises with the classical formulation is presented and discussed in Section III. Section IV elaborates the proofs, properties and suitability of the proposed new mathematical framework. Section V assesses the performance in a real-case scenario with SAR data. Finally, Section VI summarizes the study with conclusions, limitations and directions of future work.

II. Classical theory of ratio change statistics

The classical theory of pixel-based change detection by means of a test statistic considers multilook SAR intensity images that are co-registered, calibrated, with the same observation geometry, and with the same number of pixels [39]. That is often the case for observations carried out with the same radar sensor, usually in a repeat-pass configuration, and will hereafter be referred to as the reference configuration. Since the images are produced by the same instrument and with the same geometry, their spatial resolutions are equal, and hence they usually undergo the same level of incoherent multilooking as an image reconstruction processing step to mitigate speckle fluctuations [40]. In its simplest form and for homogeneous terrain, the pixel values of the histogram of a multilook SAR intensity image are outcomes of a Gamma random variable, distributed as:

$$p(x;\alpha,\theta)=\frac{1}{\theta^{\alpha}\Gamma(\alpha)}x^{\alpha-1}e^{-\frac{x}{\theta}} \quad x>0 \quad \alpha,\theta>0 \quad (1)$$

where x is a measure of the SAR intensity, often the backscattering coefficient σ_0, α is the shape parameter corresponding to the number of looks L applied to the image, and θ is the scale parameter corresponding to the mean intensity value of the image σ divided by the number of looks L [39]. The Gamma model is acceptable in the context of fully developed speckle, which implies scatterer-independent amplitude and phase (the phase being uniformly distributed) [25]. This is applicable to homogeneous areas where there is the assumption of large numbers of statistically identical scatterers.

A SAR image usually presents a degree of pixel correlation because the pixel spacing must be smaller than the spatial resolution; to avoid aliasing and loss of information, the pixel spacing is typically smaller by at least the broadening factor, determined by the spectra window that is applied to suppress the sidelobes of the SAR point target response. To account for this, the L value typically used in (1) is the Equivalent Number of Looks, $ENL=\frac{mean^2}{variance}$, which is an estimate of the number of independent looks of the image [39].

The core idea of the test statistic is to identify and classify pixels as "change" and "no-change" classes by means of the selection of a threshold value that separates them. This strategy suffices after identifying whether the change increases or decreases the SAR intensity. The threshold is a single value of a metric that compares the images pixel-to-pixel, and since such metric is always governed by the gamma-distributed nature of multilook SAR images, its selection necessarily implies a certain misclassification error, commonly referred to as false alarm rate. A pixel-wise image subtraction approach is not suitable for SAR images since the selection of a threshold would yield a variable false alarm rate depending on the σ_0 values of the pixels [41]; to ensure a single Constant False Alarm Rate (CFAR) across the change metric, the ratio of the images, referred to as image ratio, is to be used [39].

Consider two uncorrelated SAR σ_0 images I_1 and I_2 with reference configuration and the same number of looks L. Their ratio image R is then a distributed metric known to follow the following probability density function [39]:

$$p(R)=\frac{\Gamma(2L)}{\Gamma^2(L)}\frac{\gamma^L R^{L-1}}{(\gamma+R)^{2L}} \quad (2)$$

where $\gamma=\frac{\sigma_2}{\sigma_1}$ is the ratio of the mean values of the images.

For established values of $\alpha=L$ and γ, the detection probability P_d above a threshold T can be found by integrating (2) with respect to the ratio value R:

$$P_d(T,L)=p\{R>T\}=\int_T^{\infty}p(R)dR=\frac{\Gamma(2L)}{\Gamma^2(L)} \cdot\sum_{k=0}^{L-1}\binom{L-1}{k}\frac{(-1)^{L-k-1}}{2L-k-1}\left(1+\frac{T}{\gamma}\right)^{k-2L+1} \quad (3)$$

Authorized licensed use limited to: Imperial College London. Downloaded on March 01,2024 at 10:36:50 UTC from IEEE Xplore. Restrictions apply.
© 2024 IEEE. Personal use is permitted, but republication/redistribution requires IEEE permission. See https://www.ieee.org/publications/rights/index.html for more information.

This article has been accepted for publication in IEEE Transactions on Geoscience and Remote Sensing. This is the author's version which has not been fully edited and content may change prior to final publication. Citation information: DOI 10.1109/TGRS.2024.3369509

where $\binom{L-1}{k}$ is a binomial coefficient and L is an integer value to satisfy the discrete summation of terms in (3). The typical procedure to approach change classification is to select a maximum CFAR or misclassification error P_e between "change" and "no-change" classes. This error can be calculated by assuming "no-change", i.e. by setting $\gamma = 1$ in (3), and depends on the number of looks L chosen [39]. On the other hand, the number of looks, together with the value of γ and the choice of T, settles a detection probability P_d. Since γ is given by the characteristics of I_1 and I_2, the aim is to find the optimal values of T and L that provide high P_d values, ideally 95-98 %, while keeping the CFAR below 5 % (one pixel out of a 4×5 pixel patch will be misclassified). The larger the number of looks, the lower the achievable CFAR, but at the cost of spatial resolution.

In practice, local σ_0 changes between two images produce a secondary component of values in the histogram (encompassing both changed and unchanged pixels), with a mean value displaced with respect to the majority of the pixels, which are distributed around a mean value close to unity. The histogram becomes then a mixture of two components with a bimodal behaviour, which can be fit using two different distributions following (2). When this bimodal histogram scenario occurs, the two components tend to overlap (unless the change is very sharp), and the threshold can be automatically chosen by means of an optimization method such as the maximum likelihood classification with the assumption of equal *a priori* probabilities [2] or the Otsu method [42].

The number of looks L is then the only free parameter that governs the P_d and P_e linked with the threshold T of each distribution. Notice that, by doing so, the optimization method is what settles the threshold value and therefore, the misclassification error, and not vice versa. If that happens, one strategy is that the error associated with the optimal threshold is always below a fixed CFAR such as 5 %. In any case, both components in the histogram should present shapes that can be fit with (2), and associated probabilities above the threshold found using (3); the presented framework can therefore be utilized in any real context that preserves the assumptions of the equations.

As a final note in this regard, it is worth mentioning that the applicability of this statistical framework relies on an adequate pixel sample; the image size and the extent of the changes within it is a limiting factor of the method. Images too small might not provide enough data for statistical inference, and the same applies to the extent of the changes in relation to their size; the detected changes should cover a sufficiently large population of pixels for the change distribution to be discernable, as well as have a distinct-enough mean value. On another hand, the assumption of terrain homogeneity should hold; too large an image would most likely bring a range of radiometric values so wide, that change would be undetectable. Therefore, the method presents a marked sensibility on the image and change sizes, and further studies about it are encouraged when attempting to apply the method to specific cases.

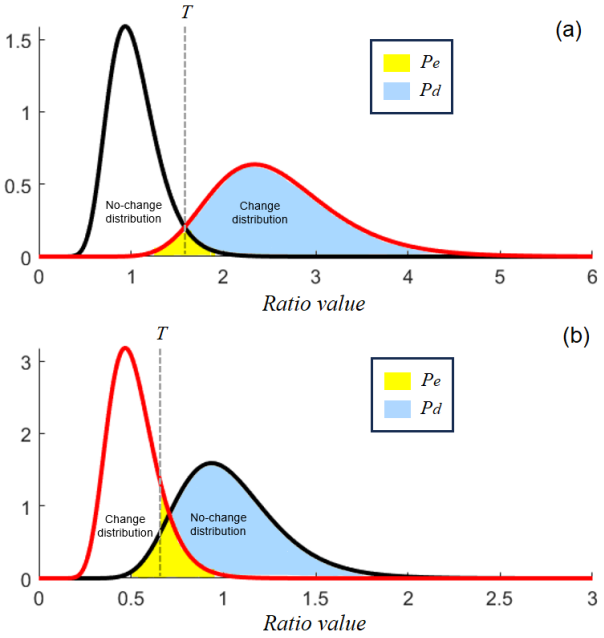


Fig. 1. Examples of likely scenarios for test statistic distribution fits according to (2), fitting the likely shape of the ratio histogram, in a case of substantial, localized change between two SAR images (to higher (a) or lower (b) σ_0 values). The constant probability of misclassification (or CFAR) in these cases corresponds to the yellow area under the curves, while the detection probability as defined in (3) corresponds to the area in blue. The threshold values T are found with the equal-probability assumption (a) and the Otsu method (b).

III. Problem Formulation

The typical scenario of SAR change detection with tests statistics, introduced in Section II, concerns the comparison of imagery from the same radar sensor, with the images having comparable spatial resolution and

Authorized licensed use limited to: Imperial College London. Downloaded on March 01,2024 at 10:36:50 UTC from IEEE Xplore. Restrictions apply.
© 2024 IEEE. Personal use is permitted, but republication/redistribution requires IEEE permission. See https://www.ieee.org/publications/rights/index.html for more information.

This article has been accepted for publication in IEEE Transactions on Geoscience and Remote Sensing. This is the author's version which has not been fully edited and content may change prior to final publication. Citation information: DOI 10.1109/TGRS.2024.3369509

pixel spacing. This is not a likely scenario, however, if considering SAR imagery of other planetary bodies on the solar system; considering the trend of spatial resolution improvement of the last 2-3 decades for SAR imaging systems on Earth, and the scarcity of planetary SAR missions, inter-mission image comparison will likely deal with images with very different spatial resolution, and consequently pixel spacing.

Such is the case for future comparisons between the SAR imagery to be generated by the VenSAR and VISAR instruments on board EnVision [33] and VERITAS [34], respectively, and the Magellan data compiled in the 1990s: with an approximately 40 year baseline between them, Magellan SAR spatial resolution was of 120-360 m in range [32] and presented a 75 m pixel spacing, while future VenSAR spatial resolution is planned to be as good as 10 m in high resolution stripmap mode and VISAR should provide a 15 m resolution with 7 looks of around 20 % of the surface of Venus [38]. Their pixel spacing is consequently expected to be also finer.

To pursue the pixel-based change detection method described in Section II, the two images considered must necessarily have the same pixel spacing and number of looks L. Moreover, the case of different spatial resolutions entails that in practice, the one with the lowest resolution constitutes the limit of the scale of the changes that could be detected in the change detection process. One way to address this imbalance is to apply a different level of incoherent averaging to each image in the speckle reduction process, and then decimate the finer resolution image to the same pixel spacing of the coarser resolution one. This procedure would achieve a large pixel spacing, in line with the image of coarser resolution, but consequently the two images would have different number of looks, L_1 and L_2, respectively. Another strategy would be to apply an FFT-interpolation to upsample the coarser resolution image to the same pixel spacing of the finer resolution one. This would produce a pixel-to-pixel comparison of images with a finer pixel spacing and potentially with the same number of looks, depending on the characteristics of the sensors, but with very different spatial resolutions.

Both methods could procure pixel-to-pixel matches in the coregistration process, while the first would be much less computationally complex. However, since the change detection output resolution is defined by the coarser of the two input resolutions, a pixel spacing the size of the finer resolution image would be unnecessarily oversampling. Moreover, increasing the number of looks for the finer resolution image does not have any drawbacks, while it maximizes the number of looks, i.e. minimizes the standard deviation and improves the ability to detect potential changes.

Therefore, consider two co-registered, calibrated SAR intensity images, with the same pixel size after a decimation process, but presenting different number of looks. In addition, their radar carrier frequency is different, precluding any coherent correlation effects between them. Their associated gamma probability density functions, as defined in (1), can be written as:

$$p(I_2, L_2, \frac{L_2}{\sigma_2}) = \frac{1}{\Gamma(L_2)} \left(\frac{L_2}{\sigma_2}\right)^{L_2} I_2^{L_2-1} e^{-\frac{L_2 I_2}{\sigma_2}} \quad (4)$$

$$p(I_1, L_1, \frac{L_1}{\sigma_1}) = \frac{1}{\Gamma(L_1)} \left(\frac{L_1}{\sigma_1}\right)^{L_1} I_1^{L_1-1} e^{-\frac{L_1 I_1}{\sigma_1}} \quad (5)$$

The formulation of a generalized version of the theory introduced in Section II able to account for differences between L_1 and L_2 is subsequently addressed.

IV. Generalized Beta Prime Distribution

Consider two variables X_k which are independent. This is generally the case for two SAR intensity images acquired with different carrier frequencies and disjoint spectra, because full decorrelation occurs. Consider also that they are both gamma distributed such as $X_k \sim \Gamma(\alpha_k, \theta_k)$ with different shape and scale parameters, in line with Section II. It has been proven [43], [44] that the probability density function of the ratio image $\frac{X_2}{X_1}$ between the two follows a generalized beta prime distribution, also referred to as generalized inverse beta function, generalized beta function of second kind or *GB2*, of the form $\frac{X_2}{X_1} \sim \beta'(\alpha_2, \alpha_1, 1, \frac{\theta_2}{\theta_1})$. The generalized beta prime distribution can be theoretically described with the following equation [44]:

$$p(x; a, b, p, q) = \frac{p(\frac{x}{q})^{ap-1} \left(1 + (\frac{x}{q})^p\right)^{-(a+b)}}{qB(a, b)} \quad (6)$$

where $B(a, b)$ is the well-known beta function. Substituting and rearranging the terms, with $a = \alpha_2 = L_2$, $b = \alpha_1 = L_1$, $p = 1$ and $q = \frac{\theta_2}{\theta_1} = \frac{L_1\sigma_2}{L_2\sigma_1}$, the probability density function of the ratio image $R = x = \frac{I_2}{I_1}$ is:

$$\begin{aligned} p(R) &= p\left(R; L_2, L_1, 1, \frac{L_1\sigma_2}{L_2\sigma_1}\right) \\ &= \frac{\rho^{L_2} R^{L_2-1}}{B(L_2, L_1)\,(1+\rho R)^{(L_2+L_1)}} \\ &\quad R, L_2, L_1, \rho > 0 \end{aligned} \quad (7)$$

Authorized licensed use limited to: Imperial College London. Downloaded on March 01,2024 at 10:36:50 UTC from IEEE Xplore. Restrictions apply.
© 2024 IEEE. Personal use is permitted, but republication/redistribution requires IEEE permission. See https://www.ieee.org/publications/rights/index.html for more information.

This article has been accepted for publication in IEEE Transactions on Geoscience and Remote Sensing. This is the author's version which has not been fully edited and content may change prior to final publication. Citation information: DOI 10.1109/TGRS.2024.3369509

with the parameter ρ being defined as the inverse of q; a look-normalized version of the inverse of the ratio of the mean of the images γ:

$$\rho = \frac{1}{q} = \frac{L_2\sigma_1}{L_1\sigma_2} = \frac{L_2}{L_1}\frac{1}{\gamma} \tag{8}$$

The generalized beta prime distribution will be defined with the parameters L_2, L_1 and ρ, and the numerator image is to be referred to with the subscript 2 while the denominator one with subscript 1.

Equation (7) is initially found to be valid according to Section II, as it can be shown to be a generalization of (2) when $L_2 = L_1 = L$ and $\gamma = \frac{\sigma_2}{\sigma_1} = \frac{1}{\rho}$, i.e. when the two images are composed in the same way and can be considered to have the same or similar image statistics:

$$\begin{aligned} p(R) &= \frac{\rho^L R^{L-1}}{B(L,L)(1+\rho R)^{2L}} = \frac{1}{B(L,L)} \\ &\cdot \frac{R^{L-1}}{\gamma^L(1+\frac{R}{\gamma})^{2L}} = \frac{1}{B(L,L)}\frac{\gamma^{2L}R^{L-1}}{\gamma^L(\gamma+R)^{2L}} \end{aligned} \tag{9}$$

Since $B(L,L) = \frac{\Gamma(L)\Gamma(L)}{\Gamma(L+L)} = \frac{\Gamma^2(L)}{\Gamma(2L)}$:

$$p(R) = \frac{\Gamma(2L)}{\Gamma^2(L)}\frac{\gamma^L R^{L-1}}{(\gamma+R)^{2L}} \tag{10}$$

The generalized beta prime distribution is an absolutely continuous univariate distribution associated with a random variable x, in this case the ratio intensity R, and as such it has to be non-negative, continuous and integrable to 1 [43]. Equation (7) states that the ratio R, the number of looks L_2 and L_1 and ρ must be larger than zero, and this is always the case in the proposed situation. The number of looks L_2 or L_1 of a SAR intensity image is always larger than zero per definition, and *R* is always necessarily larger than zero since the SAR intensity values are positive, finite values, if the images are well calibrated.

SAR intensity values can in specific cases be manipulated prior to multilooking, for instance in noise subtraction steps. In other cases, the raw pixel intensity values of the images might be log transformed and scaled. This is the case of Magellan SAR measurements, where the data has undergone dynamic range compression and correction due to latitude-varying differences in incidence angle by means of the empirical law derived by Muhleman [45]. In these cases, it is necessary to retrieve a corrected and linear SAR intensity form, typically σ_0, which should ensure the real, positive pixel values necessary for the correct application of the *GB2* framework. The statistics presented should nevertheless hold for any other form of SAR intensity such as radar cross-section or other normalized coefficients such as β_0 and γ_0, as long as the data is in linear form and has been averaged to a certain degree.

The non-negativity, continuity and integration of the *GB2* function is generally known; a demonstration of the area under the curve being equal to 1 is presented in Appendix A to address the results of Section IV-B.

A. Properties of interest

Having corroborated the theoretical suitability of the *GB2* distribution, knowledge of the shape of the distribution is important for two reasons: first, to corroborate that its behaviour is consistent with the properties of the classical result in (2), and second, to be able to use it to fit the ratio-derived histogram with accuracy in a practical case. The mean value of the *GB2* distribution μ_1 is the first raw moment, which can be calculated by setting $n = 1$, and considering the values of a, b, p and q as in (7), in the following expression defined in [44]:

$$\mu_n = \frac{q^n B(a+\frac{n}{p}, b-\frac{n}{p})}{B(a,b)} = \frac{B(L_2+n, L_1-n)}{\rho^n B(L_2,L_1)} \tag{11}$$

$$\begin{aligned} \mu_1 &= \frac{B(L_2+1, L_1-1)}{\rho B(L_2,L_1)} = \frac{\frac{\Gamma(L_2+1)\Gamma(L_1-1)}{\Gamma(L_2+L_1)}}{\rho\frac{\Gamma(L_2)\Gamma(L_1)}{\Gamma(L_2+L_1)}} \\ &= \frac{\sigma_2 L_1}{\sigma_1 L_2}\frac{\Gamma(L_2+1)\Gamma(L_1-1)}{\Gamma(L_2)\Gamma(L_1)} \end{aligned} \tag{12}$$

Since $\Gamma(z+1) = z\Gamma(z)$, then $\Gamma(L_2+1) = L_2\Gamma(L_2)$. Furthermore, using the definition of the Gamma function $\Gamma(z) = (z-1)!$, it follows that $\frac{\Gamma(L_1-1)}{\Gamma(L_1)} = \frac{(L_1-2)\cdot(L_1-3)\cdot\ldots\cdot(L_1-L_1+1)}{(L_1-1)\cdot(L_1-2)\cdot\ldots\cdot(L_1-L_1+1)} = \frac{1}{L_1-1}$. Using these results in (12) yields:

$$\mu_1 = \frac{\sigma_2 L_1}{\sigma_1 L_2}\frac{L_2\Gamma(L_2)}{\Gamma(L_2)(L_1-1)} = \frac{\sigma_2}{\sigma_1}\frac{L_1}{L_1-1} \tag{13}$$

This result is remarkable, and it shows that the mean value of the distribution depends on the ratio of the means of the intensity images and on the denominator image number of looks only. The larger the number of looks L_1, the less deviation the mean suffers from the $\frac{\sigma_2}{\sigma_1}$ ratio, implying that the number of looks L_1 acts as the sole modulator of the ratio mean independently of L_2. Fig. 2 illustrates this behaviour using a numerical simulation of the ratio of two Gamma-distributed sets of $N = 10^4$ randomly-generated samples.

Authorized licensed use limited to: Imperial College London. Downloaded on March 01,2024 at 10:36:50 UTC from IEEE Xplore. Restrictions apply.
© 2024 IEEE. Personal use is permitted, but republication/redistribution requires IEEE permission. See https://www.ieee.org/publications/rights/index.html for more information.

This article has been accepted for publication in IEEE Transactions on Geoscience and Remote Sensing. This is the author's version which has not been fully edited and content may change prior to final publication. Citation information: DOI 10.1109/TGRS.2024.3369509

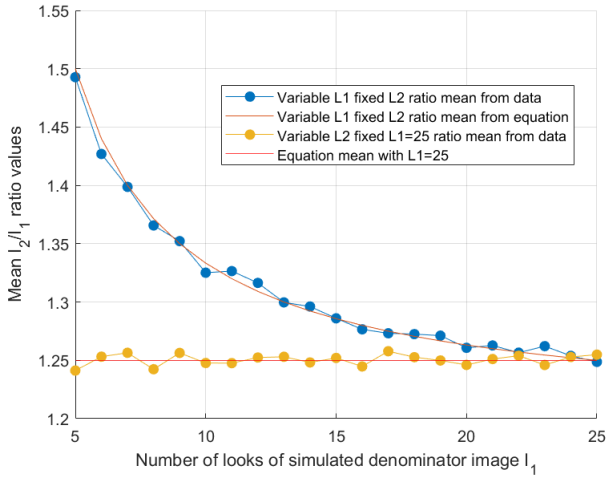


Fig. 2. *GB2* mean value μ_1 simulation with variable L_1 and L_2 number of looks from randomly-generated Gamma distributions of mean values $\sigma_1 = 0.025$ and $\sigma_2 = 0.03$, respectively. The ratio mean values calculated from the data and (13) match well, and they are constant for a fixed value of $L_1 = 25$ regardless of variations in L_2, corroborating the implications of (13).

In addition, and perhaps more critical to the fitting process, the "peaky" behaviour of the distribution is corroborated, and the location and value of the peak analytically derived. The first derivative of (7) is:

$$\frac{dp(R)}{dR} = \frac{\rho^{L_2}}{B(L_2,L_1)} \frac{L_2-1}{(1+\rho R)^{2L_2+2L_1}} \frac{R^{L_2-2}(1+\rho R)^{L_2+L_1}}{(1+\rho R)^{2L_2+2L_1}} \cdot \frac{-R^{L_2-1}(L_2+L_1)\rho(1+\rho R)^{L_2+L_1-1}}{(1+\rho R)^{2L_2+2L_1}} \tag{14}$$

By means of the first derivative test to find relative extrema, $\frac{dp(R)}{dR} = 0$, it follows that:

$$(L_2-1)R^{L_2-2}(1+\rho R)^{L_2+L_1} - R^{L_2-1}(L_2+L_1)\rho(1+\rho R)^{L_2+L_1-1} = 0 \tag{15}$$

Then, rearranging, the value of *R* that satisfies this condition is:

$$R^{L_2-1}(1+\rho R)^{L_1+L_2}\left(\frac{L_2-1}{R} - \frac{\rho(L_2+L_1)}{1+\rho R}\right) = 0 \tag{16}$$

$$L_2 + L_2\rho R - 1 - \rho R = \rho(L_2+L_1)R \tag{17}$$

$$R_{peak} = \frac{L_2-1}{\rho(L_1+1)} \tag{18}$$

This point R_{peak} is in fact a global maximum of the function, with the corresponding image $p(R_{peak})$:

$$\begin{aligned} p(R_{peak}) &= \frac{\rho^{L_2}}{B(L_2,L_1)} \frac{x_m^{L_2-1}}{(1+\rho x_m)^{L_2+L_1}} \\ &= \frac{\rho^{L_2}}{B(L_2,L_1)} \frac{\left(\frac{L_2-1}{\rho(L_1+1)}\right)^{L_2-1}}{\left(\frac{L_1+L_2}{L_1+1}\right)^{L_2+L_1}} \\ &= \frac{\rho^{L_2}}{B(L_2,L_1)} \frac{(L_1+1)^{L_1+1}(L_2-1)^{L_2-1}}{(L_1+L_2)^{L_2+L_1}} \end{aligned} \tag{19}$$

This point constitutes a maximum because the second derivative evaluated in it is negative, as illustrated in appendix B. Higher order moments provide more information about the shape of the distribution, and can be derived from (11) by choosing other integer values of $n > 0$.

B. Associated Cumulative Distribution Function

The cumulative distribution function (CDF) associated with a generalized beta prime distribution is [44]:

$$F(x;a,b,p,q) = \frac{\left(\frac{\left(\frac{x}{q}\right)^p}{1+\left(\frac{x}{q}\right)^p}\right)^a}{aB(a,b)} \cdot {}_2\mathrm{F}_1\left[a, 1-b; a+1; \frac{\left(\frac{x}{q}\right)^p}{1+\left(\frac{x}{q}\right)^p}\right] \tag{20}$$

where the term ${}_2F_1$ refers to the Gaussian hypergeometric function. Equation (20) can be described with the particular nomenclature of the *GB2* as in (7):

$$F(R;L_2,L_1,1,\frac{1}{\rho}) = \frac{\left(\frac{\rho R}{1+\rho R}\right)^{L_2}}{L_2 B(L_2,L_1)} \cdot {}_2\mathrm{F}_1\left[L_2, 1-L_1, L_2+1; \frac{\rho R}{1+\rho R}\right] \tag{21}$$

For given L_2, L_1, σ_2 and σ_1, the detection probability can be defined for this case analogously as in the classical theory of Section II, following (3):

$$\begin{aligned} P_d(T,L_2,L_1) &= P\{R > T\} = \int_T^\infty p(R)dR \\ &= \frac{\rho^{L_2}}{B(L_2,L_1)} \cdot \int_T^\infty \frac{R^{L_2-1}}{(1+\rho R)^{L_2+L_1}} dR = \\ & F(\infty;L_2,L_1,1,\frac{1}{\rho}) - F(T;L_2,L_1,1,\frac{1}{\rho}) \end{aligned} \tag{22}$$

Authorized licensed use limited to: Imperial College London. Downloaded on March 01,2024 at 10:36:50 UTC from IEEE Xplore. Restrictions apply.
© 2024 IEEE. Personal use is permitted, but republication/redistribution requires IEEE permission. See https://www.ieee.org/publications/rights/index.html for more information.

This article has been accepted for publication in IEEE Transactions on Geoscience and Remote Sensing. This is the author's version which has not been fully edited and content may change prior to final publication. Citation information: DOI 10.1109/TGRS.2024.3369509

This result can be simplified but requires the formulation of the Gaussian hypergeometric function in its general form [46]:

$$
\begin{aligned}
{}_2F_1\left[a,b;c;x\right] &= \sum_{n=0}^{\infty}\frac{(a)_n(b)_n}{(c)_n}\frac{x^n}{n!}\\
(q)_n &= \begin{cases} 1 & n=0 \\ q(q+1)...(q+n-1) & n>0 \end{cases}
\end{aligned}
\tag{23}
$$

where $(q)_n$ is the Pochhammer function or rising factorial. $F(\infty; L_2, L_1, 1, \frac{1}{\rho}) = 1$ is a known result, the derivation of which can be found in Appendix A, but $F(T; L_2, L_1, 1, \frac{1}{\rho})$ depends on the value of T such as:

$$
\begin{aligned}
F(T; L_2, L_1, 1, \frac{1}{\rho}) &= \frac{\delta^{L_2}}{L_2 B(L_2, L_1)}\\
\cdot {}_2F_1\left[L_2, 1-L_1; L_2+1; \delta\right] &= \frac{\delta^{L_2}\Gamma(L_2+L_1)}{\Gamma(L_2)\Gamma(L_1)L_2}\\
\cdot \sum_{n=0}^{\infty}\frac{(L_2)_n(1-L_1)_n}{(L_2+1)_n}\frac{\delta^n}{n!}&
\end{aligned}
\tag{24}
$$

where δ is the threshold-dependent variable defined as:

$$
\delta = \frac{\rho T}{1+\rho T} \tag{25}
$$

In the special cases of the ${}_2F_1$ function when one of the numerators a or b, $b = 1 - L_1$ in this case, is a non-positive integer, the sum is bounded. The function is then constructed as stated in [47]:

$$
{}_2F_1(a, b<0; c; x) = \sum_{n=0}^{-b}\frac{(a)_n(b)_n}{(c)_n}\frac{x^n}{n!} \tag{26}
$$

Substituting this change in (24) yields:

$$
\begin{aligned}
F(T; L_2, L_1, 1, \frac{1}{\rho}) &= \frac{\delta^{L_2}\Gamma(L_2+L_1)}{\Gamma(L_2)\Gamma(L_1)L_2}\\
\cdot \sum_{n=0}^{L_1-1}\frac{(L_2)_n(1-L_1)_n}{(L_2+1)_n}\frac{x^n}{n!}&
\end{aligned}
\tag{27}
$$

Since $(x)_n = \frac{\Gamma(x+n)}{\Gamma(x)}$ and $\Gamma(x+1) = x\Gamma(x)$, then:

$$
\frac{(q)_n}{(q+1)_n} = \frac{\frac{\Gamma(q+1)}{\Gamma(q)}}{\frac{\Gamma(q+2)}{\Gamma(q+1)}} = \frac{q}{q+n} \tag{28}
$$

Substituting this result in (27) yields:

$$
\begin{aligned}
F(T; L_2, L_1, 1, \frac{1}{\rho}) &= \frac{\delta^{L_2}\Gamma(L_2+L_1)}{\Gamma(L_2)\Gamma(L_1)L_2}\\
&\cdot \sum_{n=0}^{L_1-1}\frac{L_2(1-L_1)_n}{L_2+n}\frac{\delta^n}{n!}\\
&= \frac{\delta^{L_2}\Gamma(L_2+L_1)}{\Gamma(L_2)\Gamma(L_1)}\sum_{n=0}^{L_1-1}\frac{(1-L_1)_n}{L_2+n}\frac{\delta^n}{n!}
\end{aligned}
\tag{29}
$$

This analytical expression, presenting a finite sum of terms, can already be computed. However, it is advisable to come up with a computation strategy to deal with very large numbers with a mathematical precision that suffices to calculate $F(T; L_2, L_1, 1, \frac{1}{\rho})$. Considering the result in (29), the detection probability P_d above a threshold value T is found by restating (22) as:

$$
\begin{aligned}
P_d(\delta, L_2, L_1) &= 1 - \frac{\delta^{L_2}\Gamma(L_2+L_1)}{\Gamma(L_2)\Gamma(L_1)}\\
&\cdot \sum_{n=0}^{L_1-1}\frac{(1-L_1)_n}{L_2+n}\frac{\delta^n}{n!}
\end{aligned}
\tag{30}
$$

C. Analysis with simulated data

Before attempting to use the presented formulation with real SAR data, analysis of a simple simulation is helpful to assess the suitability of the method, and to highlight the improvement it brings with respect to the classic formulation with a single L value, as introduced in Section II. The capacity of both methods to calculate the change and error probabilities, P_d and P_e, ultimately depends on how well they fit the data; therefore, a basic statistical assessment of the goodness of fit should provide a useful evaluation metric.

Two sets of 10^5 gamma-distributed values with unit mean and shape values $L_1 = 10$ and $L_2 = 100$ were generated and then divided, producing a simulated ratio SAR image of an assumed homogeneous area, imaged twice with averaging levels differing by an order of magnitude (as expected between Magellan and VenSAR/VISAR). The resulting histogram of the ratio data has been fit with *GB2* using (9) with the L_2 and L_1 values as above. In parallel, a series of fits have been computed using (2) and compared to GB2. Since the data has been constructed by ratioing two simulated SAR intensity images averaged with very different number of looks L, there is no unique L value that is equivalent for use in (2), since the assumption of the same number of looks for both images/datasets does not hold.

Authorized licensed use limited to: Imperial College London. Downloaded on March 01,2024 at 10:36:50 UTC from IEEE Xplore. Restrictions apply.
© 2024 IEEE. Personal use is permitted, but republication/redistribution requires IEEE permission. See https://www.ieee.org/publications/rights/index.html for more information.

This article has been accepted for publication in IEEE Transactions on Geoscience and Remote Sensing. This is the author's version which has not been fully edited and content may change prior to final publication. Citation information: DOI 10.1109/TGRS.2024.3369509

All possible L values between L_1 and L_2 have been considered, to generate fits of the data, and to find a compromise value that lies between them. For each of the fits, including *GB2*, basic regression analysis statistical measures have been computed as a preliminary estimation of the quality of fit [48]; the general form of the coefficient of determination (R^2), the root-mean-square error (*RMSE*), and the mean absolute error (*MAE*). The point-to-point residual between fit and data has also been computed for the *GB2* fit and for the best fit generated with (2), to provide a graphical comparison between them.

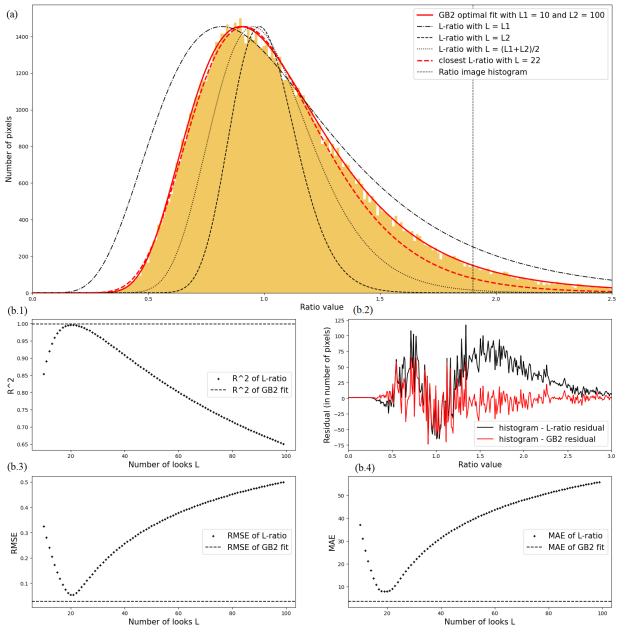


Fig. 3. Simulated data performance test of the *GB2* framework compared to the L-ratio of the classic theory computed with (2): (a) shows a compilation of fits, including *GB2* and several L-ratio. *GB2* exhibits a perfect fit, while the closest L-ratio fit with $L = 22$ is unable to precisely define the trailing edge of the histogram. (b.1-4) presents a compilation of several statistic metrics to assess the goodness of the L-ratio fits, for different values of L, with respect to *GB2*. A close-enough fit is found with a compromise value $L = 22$, but *RMSE* (b.3) and *MAE* (b.4) scores are worse than those of the *GB2* fit. Moreover, it does not follow the data as well as *GB2* throughout all the span, as evidenced by higher values of the residual (b.2).

Fig. 3 exposes the theoretical superiority of the new *GB2* framework with respect to the classic L-ratio using (2). The L_1 and L_2 values used to generate the simulated data can be used directly to generate a *GB2* fit that perfectly matches the ratio image histogram. On the contrary, the classic L-ratio cannot be used rigorously, as it does not consider different averaging levels. Moreover, the best-fit approximation obtained (*L=22*) yields a result with a lower performance with respect to that of the *GB2*. The goodness of that fit is similar if comparing the R^2 results of Fig. 3(b.1), but it is worse in terms of *RMSE* and *MAE*, shown in Figs. 3(b.3) and 3(b.4) respectively, as well as particularly failing to match the trailing edge of the histogram as shown in the residual plot in Fig. 3(b.4). These results support the claim that even if mathematically correct for the case, the new framework also outperforms any adjusted version of the classic L-ratio fit, adapting to the leading and trailing edges of the data more independently.

V. Performance Assessment with Magellan SAR Data

Magellan SAR backscatter σ_0 data is the best resolution imagery, to date, of the surface of Venus [32]. To simulate future VISAR/VenSAR-Magellan image comparison by means of a pixel-to-pixel test statistic, co-registration, decimation and orthorectification prior to the ratio operation are assumed, making the images geometrically and radiometrically comparable, and thus facilitating the matching of features between them. No radiometric distortions due to differences in carrier frequency, polarisation or thermal noise between the images are considered.

Two tests have been conducted; one selecting a quasi-homogeneous area, where a single terrain unit is inferred from visual inspection and hence Gamma fitting according to Section II should in principle hold, and a second case using a larger, heterogeneous area of Venus's surface where multiple terrain units and degrees of textural complexity are included. An additional simulation, presenting an example of a possible real change occurred in the area selected for the heterogeneous case, is also included. The same Magellan SAR image from the Full-Resolution Mosaicked Image Data Record (F-MIDR) [49] is used as numerator (I_2) and denominator (I_1) in all cases. However, to simulate the expected differences in spatial resolution as stated in Section III the numerator image I_2, corresponding to the future VISAR/VenSAR image, has been processed with a 7×7 boxcar filtering operation, whilst a smaller degree of multilooking using a 3×3 version has been applied to the denominator, which plays its own Magellan role.

Authorized licensed use limited to: Imperial College London. Downloaded on March 01,2024 at 10:36:50 UTC from IEEE Xplore. Restrictions apply.
© 2024 IEEE. Personal use is permitted, but republication/redistribution requires IEEE permission. See https://www.ieee.org/publications/rights/index.html for more information.

This article has been accepted for publication in IEEE Transactions on Geoscience and Remote Sensing. This is the author's version which has not been fully edited and content may change prior to final publication. Citation information: DOI 10.1109/TGRS.2024.3369509

The choice of these sizes for the boxcar filters has been made in relation to two points: one is the approximated proportion between the expected spatial resolutions of the VenSAR and VISAR instruments (in reconnaissance/global mode) and the finest Magellan resolution, obtained in equatorial latitudes. These are 30 m [38] and close to a 100 m [32], respectively (both in slant range and azimuth). However, this yields a proportion of 9:3, which is larger than the one between the chosen filter sizes. After several tests, it became evident that too large an averaging narrowed the histograms to the point where the spread was not easily detected; in consequence, the proportions were slightly reduced for visualization purposes. As long as the sizes of the boxcar filters applied to the two images differ, any other filter size combination should work well in order to test the methodology.

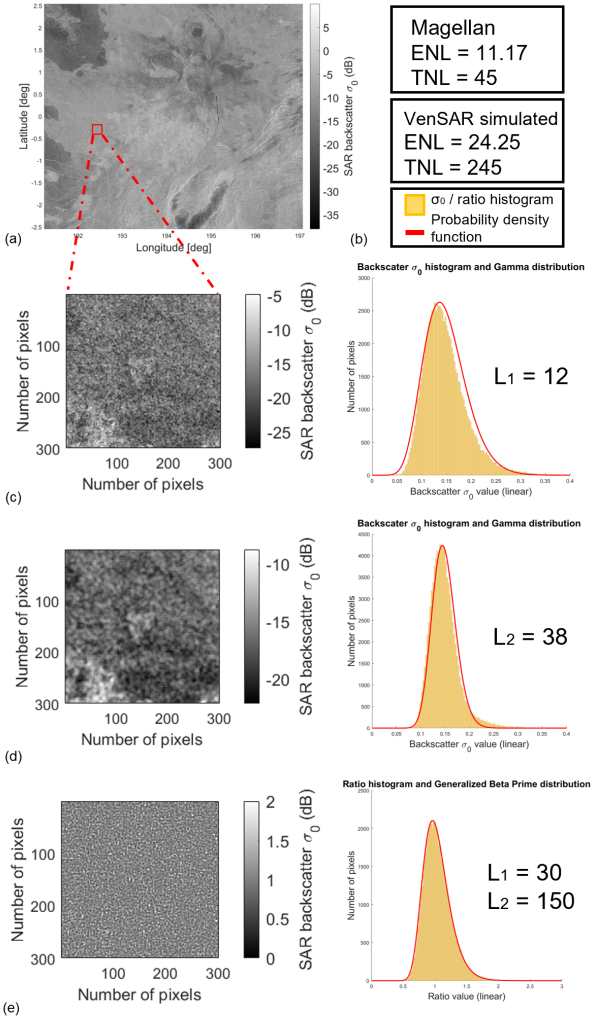


Fig. 4. Simulation showing 2 SAR multilook σ_0 images and their ratio image, with their corresponding histograms and Gamma and *GB2* fits. (a) f00n194 F-MIDR mosaic. (b) Summary of the calculated ENLs and the Total Number of Looks (TNL) applied, considering angular "burst" looks [51] and boxcar averaging, for each case. (c) The Magellan multilook image case and its corresponding Gamma histogram and fit. (d) Analogously to (c), the Magellan-derived VenSAR simulated case with a larger averaging. (e) The ratio image and its *GB2* fit.

A. *Homogeneous case*

The area selected for this test case is a 300×300 pixel portion of a lava field emplaced south-west of Atla Regio, Venus, extracted from a Muhleman-corrected σ_0 image [50] derived from the f00n194 F-MIDR mosaic [49].

Fig. 4 illustrates a relatively homogenous SAR image scene on Venus. This area contains some brightness and textural heterogeneities in its underlying σ_0 signature, which are visible in the multilook images in Fig. 4(c)-4(d). These variations drive the slight mismatch between image histograms and Gamma fit curves, producing narrower shape and slightly broader tails but with a

Authorized licensed use limited to: Imperial College London. Downloaded on March 01,2024 at 10:36:50 UTC from IEEE Xplore. Restrictions apply.
© 2024 IEEE. Personal use is permitted, but republication/redistribution requires IEEE permission. See https://www.ieee.org/publications/rights/index.html for more information.

This article has been accepted for publication in IEEE Transactions on Geoscience and Remote Sensing. This is the author's version which has not been fully edited and content may change prior to final publication. Citation information: DOI 10.1109/TGRS.2024.3369509

good overall fit. Moreover, and more importantly, these divergences do not significantly propagate to the ratio image in Fig. 4(e); the ratio histogram is excellently fit with a *GB2* distribution with $L_1 = 30$ and $L_2 = 150$. These values are much larger than the nominal looks in a Magellan F-MIDR imagery, which ranges between 5 and 17 depending on the latitude [51], but are of the order of magnitude of the expected total number of looks applied after boxcar filtering.

It is important to note that although the fits are successful in describing the overall histogram shapes, particularly for the ratio image, the values of L_1 and L_2 used in each case vary. They are in all cases different from the theoretical expected values, which should correspond with the ENLs of the images according to Section II. At the Gamma fit level, this has been theorized to be due to the inherent high correlation among pixel values of the same image. The correlation is mainly caused by two factors: first, the pixel size is smaller than the actual spatial resolution by roughly a factor of 2, making pixel pairs effectively equal, and second, the presence of textural patterns introduces an additional layer of interdependence among neighbouring pixels. Texture, understood here as a consequence of intensity fluctuations longer than the resolution, directly impacts the shape of the histograms: it distorts them away from their theoretical fits and therefore, also from the values of L_1 and L_2 used to construct them.

Considering the *GB2* fit, however, the discrepancy between the chosen L_1 and L_2 and the ENLs does not originate in the presence of intra-image correlation, but rather because of high correlation between the two images used in the ratioing operation. This occurs in the test cases of this study since, although both images have experienced different levels of averaging, they come from the same Magellan SAR measurement. The fact that the two images are therefore not independent contradicts the assumption of uncorrelated channels made in Section II, which, on the other hand, shall be true for any future use of the *GB2* framework, including for Magellan imagery comparison with future VISAR and VenSAR data. However, the results show that although *GB2* does not account for image correlation, there are in fact values of L_2 and L_1 that can generate a very good fit with *GB2*; the correlation effects can be compensated by varying the choice of number of looks.This is seen as an advantage and a useful trait of the framework; deriving an expression with different number of looks that also accounts for a certain degree of correlation is a much more complex endeavour, and it is deemed unnecessary for change detection between different SAR sensors, because of their different carrier frequencies. Therefore, a simple tuning of the L_2 and L_1 parameters is enough to successfully fit any ratio histogram from images with a level of pixel correlation.

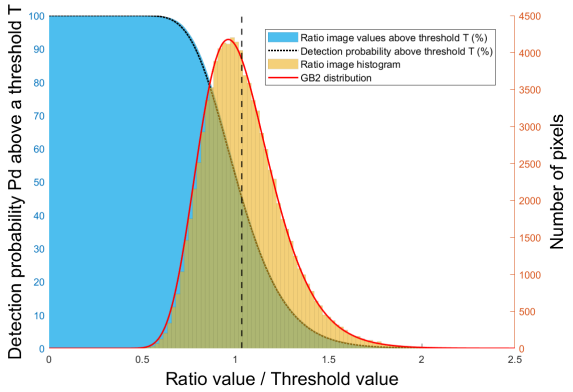


Fig. 5. The homogeneous area ratio histogram and its corresponding *GB2* fit as in Fig. 4(e), together with the corresponding associated detection probability above a ratio threshold *T* both from the image data and from the fit provided by (30), and a dashed vertical line corresponding to the mean value μ_1.

Fig. 5 shows a perfect match from the theory introduced in Section IV and the behaviour of the Magellan data. The ratio image mean value $\mu = 1.07$ matches in 95 % the theoretical expectation given by (13). This is very close to 1, as expected of the ratio of the same image, albeit with different degrees of multilooking. Actual VISAR and VenSAR images, likely to contain real surface feature changes, are expected to produce histogram components which drift away from the mean value of 1. On the other hand, the detection probability P_d derived with (30) shows a remarkable likelihood with the data: for a given threshold ratio value T, which generates a particular δ value, and the L_1 and L_2 values used to generate the *GB2* fit in Fig. 5, the results in 30 (multiplied by 100) are very close to the actual percentage of pixels above the same threshold when considering the ratio image pixel values. This consolidates the presented CDF as a solid framework to calculate P_d in real change cases with images with different number of looks. Please note that the detection probability $P_d = p\{R > T\}$ corresponds to $1 - p\{R \leq T\} = 1 - CDF$; thus the decreasing character of P_d in Fig. 5.

Considering also that, according to the theory exposed in Section II, the probability of false alarm P_e can be calculated for any *T* and *L* values by setting $\gamma = \frac{\sigma_2}{\sigma_1} = 1$, and that this is exactly the case for this test (since the

Authorized licensed use limited to: Imperial College London. Downloaded on March 01,2024 at 10:36:50 UTC from IEEE Xplore. Restrictions apply.
© 2024 IEEE. Personal use is permitted, but republication/redistribution requires IEEE permission. See https://www.ieee.org/publications/rights/index.html for more information.

This article has been accepted for publication in IEEE Transactions on Geoscience and Remote Sensing. This is the author's version which has not been fully edited and content may change prior to final publication. Citation information: DOI 10.1109/TGRS.2024.3369509

mean value of both I_2 and I_1 is the same), the framework is also proven to work for calculating CFAR.

B. Heterogeneous case

A case analogue to Section V-A, the test area is this time a larger, 1024×1024 pixel patch of heterogeneous terrain units, consisting of a network of lava flows of distinct radar brightness and inferred highly deformed ridges, east of Idunn Mons, Imdr Regio, Venus. The Muhleman-corrected σ_0 image of the area is from the f45s218 F-MIDR mosaic.

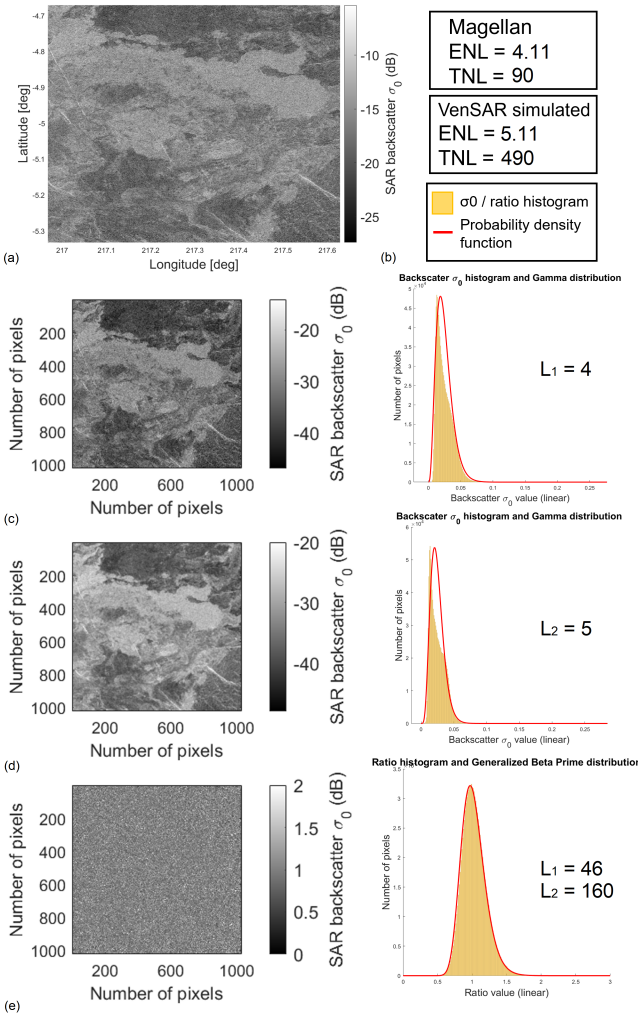


Fig. 6. Test case of 2 SAR multilook σ_0 images and their ratio image, with their corresponding Gamma and *GB2* histograms and fits. Equivalent to Fig. 4.

The results illustrated in Fig. 6 reaffirm the behaviour observed in Section V-A; an excellent fit of the ratio image histogram can be found with a *GB2* distribution, in this case using $L_1 = 46$ and $L_2 = 160$. However, specific differences arise: the disparity of terrains and the larger averaging pushes the ENLs of the area closer to the L_1 and L_2 values used for the Gamma fits. The ENL values are remarkably low compared to the TNLs, which indicates how strongly correlated the pixels are. In turn, they do not provide a good fit around the peaks of the histograms, probably because they are so low that the distribution of pixels is almost exponential. The fact that regardless of these deviations, the ratio histogram *GB2* fit works well implies that the *GB2* framework is robust even in the presence of texture, and even more so considering the fact that it does not account for a level of correlation between the images; the results show that there is a combination of L_2 and L_1 that generates a good fit independently of the weight of those factors, as seen in Section V-A.

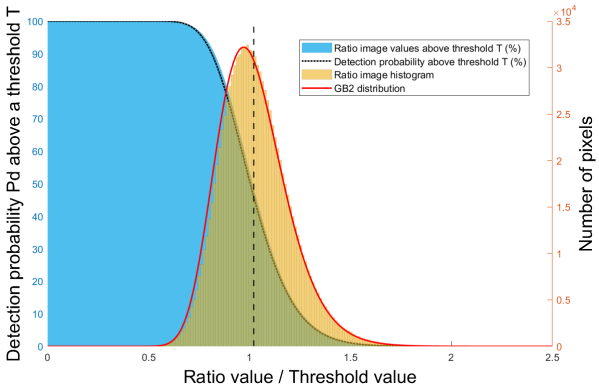


Fig. 7. Equivalent to Fig. 5, the ratio image histogram of the case and its corresponding *GB2* fit as in Fig. 6(e), superimposed with the corresponding associated CDF above a ratio threshold T, derived from the image data and from the fit provided by (30). The dashed vertical line corresponds to the theoretical mean value μ_1.

The correlation effect between images is expected to disappear in real case applications, as mentioned. However, the minimized effect of textural variations in the *GB2* histogram might be due to the textural patterns of the images being almost identical and cancelling out, since they are both Magellan images. In the case of two SAR images actually coming from different sensors, the textural patterns might vary with wavelength and look angle differences, and the *GB2* fit might not work as well in that regard. Fig. 7 also corroborates the robustness of the CDF associated with a *GB2 PDF* to provide estimates of detection probability and probability of false alarm. The fit matches very well the data behaviour, as in Fig. 5, this time in a test image patch which is heterogeneous

Authorized licensed use limited to: Imperial College London. Downloaded on March 01,2024 at 10:36:50 UTC from IEEE Xplore. Restrictions apply.
© 2024 IEEE. Personal use is permitted, but republication/redistribution requires IEEE permission. See https://www.ieee.org/publications/rights/index.html for more information.

This article has been accepted for publication in IEEE Transactions on Geoscience and Remote Sensing. This is the author's version which has not been fully edited and content may change prior to final publication. Citation information: DOI 10.1109/TGRS.2024.3369509

and has strong textural complexity across terrain units. This reinforces the claim that this generalization of the classic SAR test statistic theory is a good mathematical tool to be included in the VISAR/VenSAR-Magellan image intercomparison chain, as well as useful for any pixel-to-pixel comparison of SAR imagery with different spatial resolutions.

C. Simulated change case

Finally, to conclude the analysis on the practical uses of the *GB2* framework, one example of simulated new lava flows on top of the volcanic area introduced in Section V-B is shown below in Fig. 8.

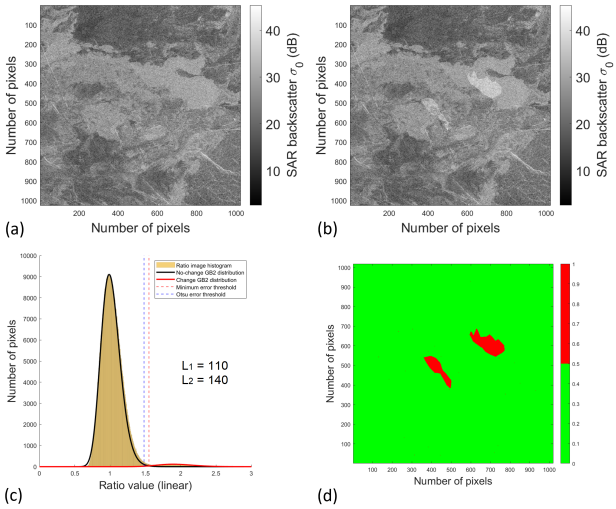


Fig. 8. Simulation of new lava flows that could be detected by VenSAR or VISAR. (a) corresponds to the multilook Magellan SAR image, as in Fig. 6. (b) represents the predicted VenSAR or VISAR image of the area, including the changes, after eventual coregistration, multilooking, decimation and orthorectification, and accounting for the system-induced changes. (c) shows the histogram shape, the *GB2* fits, and the calculated thresholds: localized changes generate a secondary, much smaller component of pixels. Finally, (d) shows the change map obtained by selecting the pixels with values above the Otsu threshold in (c).

This is a simplified, possible scenario, where either VenSAR or VISAR would register these changes in their SAR imagery. The changes have been added manually by delimiting a pair of polygons in the area point by point, and incrementing their pixels' values homogenously, multiplying by a factor of 2. The underlying speckle-remnant and textural patterns are therefore not affected by this operation, and the brightness of the "new flows" is approximately half of what the largest contrast between bright and dark patches in the neighbouring terrain is.

Fig. 8 depicts a scenario which shows how a real case application of the *GB2* framework might look like. As advanced in Section II, when one of the images involved in the test statistic presents localized changes in brightness, this appears in the ratio histogram as a secondary component. This component, comprising the pixels that are affected by change, is displaced towards the right or the left of the "main" component, which encompasses all the pixels which do not change, depending on whether the changed pixels are brighter or darker than previously. Both components are fit with *GB2* distributions using the same L_2 and L_1 parameters, but with different ρ values, as their ratio mean is different.

The choice of looks significantly differs from the theoretical expectations due to image correlation, as in Sections V-A and V-B. In the case of Fig. 8, the distributions are almost detached, making the use of optimization thresholding methodologies not so critical; regardless, only the Otsu threshold works properly. The calculated probability of detection P_d of changed pixels above the threshold is 98.08 %, and the probability of misclassification P_e is 1.92 %; Fig. 8(d) results are therefore very good according to the standards of Section II. However, more overlapping of distributions is expected for fainter σ_0 changes, and in those cases P_d would be lower and P_e would rise sharply. One way to improve change detection in those cases would be to average the images further, narrowing the spread of both distributions, but that would in turn bring less precision, because the spatial resolution would be worsened.

The ability to fit the ratio histogram with a pair of *GB2* distributions is the key step in real scenarios, and depends on several factors. These include that the change distribution has the sufficient pixels to be successfully fit, and that its radiometric mean is sufficiently distant from 1 for its peak not to fall under the umbrella of the main distribution, which would make it undetectable. The capacity to mathematically locate the peaks, as described in Section IV-A, is consequently critical for the correct description of the test statistic.

VI. Conclusions

A modification to the statistical framework of pixel-by-pixel change detection based on CFAR test

Authorized licensed use limited to: Imperial College London. Downloaded on March 01,2024 at 10:36:50 UTC from IEEE Xplore. Restrictions apply.
© 2024 IEEE. Personal use is permitted, but republication/redistribution requires IEEE permission. See https://www.ieee.org/publications/rights/index.html for more information.

This article has been accepted for publication in IEEE Transactions on Geoscience and Remote Sensing. This is the author's version which has not been fully edited and content may change prior to final publication. Citation information: DOI 10.1109/TGRS.2024.3369509

statistic has been proposed and tested with SAR data. The theory presented is based in the well-known generalized beta prime probability density function, and offers a generalization of the classical theory of the ratio of SAR intensity images, in the sense that it permits the utilization of different shape parameters or number of looks *L* to define the Gamma distributions of the two images involved in the ratio operation. In practice, this allows the test statistic method to work with images coming from radar systems that possess substantially different spatial resolutions, hence requiring different levels of averaging/multilooking for speckle reduction and resolution homogenization before pixel size decimation and the subsequent ratio operation. Therefore, the *GB2* test statistic framework allows change detection between different radar sensors, if the images are co-registered, well calibrated, and the differences arising from other divergent observational parameters are accounted for.

Tests using Magellan SAR data with different averaging levels have shown the suitability and capacity of the method to describe the ratio *PDF* and obtain detection probability estimates and CFAR. Results have shown the success of the framework in designated homogeneous areas and for large-enough blends of distinct terrain units, albeit the inferred ENL of the areas do not match the subsequent L_2 and L_1 applied to construct the equations. This is attributed to the inherent pixel correlation between the images, primarily due to both being produced from the same Magellan data; however, differences in the statistical fluctuations associated to different degrees of texture throughout the tested areas, emerging due to different averaging levels, is theorized to be a factor as well. Finally, an example of a possible simulated change scenario on the surface of Venus has been presented, showing how the *GB2* framework could be used together with thresholding methodologies to delineate changes with great accuracy.

Possible change detection applications of the *GB2* framework revolve around the comparison of SAR imagery that is completely independent due to the different sensor characteristics, both on Earth and in other planets. In that sense, the fact that the framework works well when incorporating a high degree of correlation, tuning only the L_2 and L_1 values to achieve a good fit, constitutes a proof of its adaptability and robustness. On the other hand, texture fluctuations are not assumed in the *GB2* derivation, but their impact is thought to be rather small in the results of this study because images were acquired by the same sensor. Different carrier frequencies and observation geometries are likely to drive substantial differences between the textural patterns of the images, which would distort the shape of the histograms beyond the effects seen in this study.

Therefore, a modification of the presented *GB2* framework to account for texture fluctuations could be a next step to be investigated; this might be necessary if the texture patterns of the images differ greatly, and hence the ratio operation alone is not sufficient to cancel them out. On the other hand, further tests with uncorrelated Earth Observation SAR data is also seen as a potential follow-up study to expand on the results presented here.

To conclude, in relation to a general strategy that allows SAR intermission change detection, and in particular regarding the case of VenSAR or VISAR SAR image comparison with Magellan, this study should be regarded as just one of the several building blocks necessary. Further research is needed to address the challenges of image comparison with different carrier frequencies, polarisations, and noise figures, and on how to deal with geometric and radiometric mismatches due to different observation geometries, poor geolocation and poor topography. The authors of this study are working towards this goal and would like to encourage others in its pursuit.

APPENDIX A
PROOF OF $F(\infty; L_2, L_1, 1, \frac{1}{\rho}) = 1$

A *PDF* must be continuous, non-negative and integrable to 1. These are known results for the *GB2* function, which has been used in many statistical applications [43], [44]. From (21), it follows that:

$$\begin{aligned} F(\infty; L_2, L_1, 1, \frac{1}{\rho}) &= \lim_{R\to\infty} F(R; L_2, L_1, 1, \frac{1}{\rho}) \\ &= \frac{1}{L_2 B(L_2, L_1)} {}_2\mathrm{F}_1\left[L_2, 1-L_1, L_2+1; 1\right] \end{aligned} \tag{31}$$

It is worth noticing that the variable of ${}_2\mathrm{F}_1$ in (31) is one because, as defined in (21):

$$\lim_{R\to\infty} \frac{\rho R}{1+\rho R} = 1 \tag{32}$$

This beautifully allows the application of the Gauss's summation theorem [43], which holds:

$$\begin{gathered} 2F_1(a, b; c; 1) = \frac{\Gamma(c)\Gamma(c-a-b)}{\Gamma(c-a)\Gamma(c-b)} \\ \Re(c-a-b) > 0; c \notin Z_0{}^- \end{gathered} \tag{33}$$

Authorized licensed use limited to: Imperial College London. Downloaded on March 01,2024 at 10:36:50 UTC from IEEE Xplore. Restrictions apply.
© 2024 IEEE. Personal use is permitted, but republication/redistribution requires IEEE permission. See https://www.ieee.org/publications/rights/index.html for more information.

This article has been accepted for publication in IEEE Transactions on Geoscience and Remote Sensing. This is the author's version which has not been fully edited and content may change prior to final publication. Citation information: DOI 10.1109/TGRS.2024.3369509

Since in this case $a = L_2$, $b = 1 - L_1$, $c = L_2 + 1$, and $c - a - b = L_1$ follows the condition in (31), then $2\mathrm{F}_1\left[L_2, 1 - L_1, L_2 + 1; 1\right]$ yields:

$$2F_1(L_2, 1 - L_1; L_2 + 1; 1) = \frac{\Gamma(L_2 + 1)\Gamma(L_1)}{\Gamma(1)\Gamma(L_2 + L_1)} \quad (34)$$

Since $\Gamma(1) = 1$ and $\Gamma(n + 1) = n\Gamma(n)$:

$$2F_1(L_2, 1 - L_1; L_2 + 1; 1) = \frac{L_2\Gamma(L_2)\Gamma(L_1)}{\Gamma(L_2 + L_1)} \quad (35)$$

Then, since $B(a, b) = \frac{\Gamma(a)\Gamma(b)}{\Gamma(a+b)}$, the previous equality transforms to:

$$2F_1(L_2, 1 - L_1; cL_2 + 1; 1) = L_2 B(L_2, L_1) \quad (36)$$

Substituting this result into (31) yields:

$$\begin{aligned} F(\infty; L_2, L_1, 1, \frac{1}{\rho}) &= \lim_{R\to\infty} F(R; L_2, L_1, 1, \frac{1}{\rho}) \\ &= \frac{1}{L_2 B(L_2, L_1)} \cdot L_2 B(L_2, L_1) = 1 \end{aligned} \quad (37)$$

APPENDIX B
PROOF OF LOCAL MAXIMA

Defining *f(R)* as a *GB2* function, analogue to that of (7), it follows that the second derivative with respect to *R* is:

$$\begin{aligned} \frac{d^2 f(R)}{dR^2} = \frac{\rho^{L_2}}{B(L_2, L_1)(1 + \rho R)^{4\phi}} \cdot \\ \big[(L_2 - 1)(L_2 - 2)R^{L_2 - 3}(1 + \rho R)^{3\phi} \\ -R^{L_2 - 1}\rho^2\phi(\phi - 1)(1 + \rho R)^{3\phi - 2} \\ -2\phi\rho(L_2 - 1)(1 + \rho R)^{3\phi - 1} \\ +2\phi^2\rho^2 R^{L_2 - 1}(1 + \rho R)^{3\phi - 2}\big] \end{aligned} \quad (38)$$

where $\phi = L_2 + L_1$. Extracting certain common factors and rearranging, the expression in (38) can be simplified as:

$$\frac{d^2 f(x)}{dx^2} = \frac{\rho^{L_2} R^{L_2 - 1}}{B(L_2, L_1)(1 + \rho R)^{\phi}} \cdot p_1(R) \quad (39)$$

$$\begin{aligned} p_1(R) = (L_2 - 1)(L_2 - 2)R^{-2} \\ -2(L_2 - 1)R^{-1}\phi\rho(1 + \rho R)^{-1} \\ +\phi(\phi + 1)\rho^2(1 + \rho R)^{-2} \end{aligned} \quad (40)$$

Since the first factor in (39) is always positive, the accompanying polynomial factor $p_1(R)$ can be addressed to find the sign of the complete derivative expression, substituting *R* by the peak value $R_{peak} = \frac{L_2 - 1}{\rho L_1 + 1}$:

$$\begin{aligned} p_1(R_{peak}) = \frac{(L_2 - 2)\rho^2(L_1 + 1)^2}{L_2 - 1} \\ -2\rho^2(L_1 + 1)^2 + \frac{(\phi + 1)\rho^2(L_1 + 1)^2}{\phi} \\ = \frac{\rho^2(L_1 + 1)^2(L_2 - 2)\phi - 2\rho^2(L_1 + 1)^2}{\phi(L_2 - 1)} \\ \frac{\cdot\phi(L_2 - 1) + \rho^2(1 + \phi)(L_1 + 1)^2(L_2 - 1)}{\phi(L_2 - 1)} \end{aligned} \quad (41)$$

Expression (41) can be further developed and simplified as follows, with the common factors being always positive by definition:

$$p_1(R_{peak}) = \frac{\rho^2(L_1 + 1)^2}{(L_1 - 1)\phi} p_2(R_{peak}) \quad (42)$$

$$\begin{aligned} p_2(R_{peak}) = \phi(L_2 - 2) - 2\phi(L_2 - 1) \\ +(1 + \phi)(L_2 - 1) \end{aligned} \quad (43)$$

$$\begin{aligned} p_2(R_{peak}) = \phi L_2 - 2\phi - 2\phi L_2 \\ +2\phi + L_2 + \phi L_2 - 1 - \phi = L_2 - 1 - \phi \\ = -1 - L_1 \end{aligned} \quad (44)$$

Since L_1 is always positive, the term $p(R_{peak}) = -1 - L_1$ in (44) is always negative, proving that $\frac{d^2 f(R)}{dR^2}$ evaluated in R_{peak} is a local maxima.

ACKNOWLEDGMENT

This work was produced at the Royal School of Mines, Imperial College London, following an MSc research project at the Technical University of Denmark (DTU Space). Gerard Gallardo i Peres would like to thank the European Space Agency and isardSAT S.L. for their funding and support.

REFERENCES

[1] A. K. Gabriel, R. M. Goldstein, and H. A. Zebker, "Mapping small elevation changes over large areas: Differential radar interferometry," *Journal of Geophysical Research: Solid Earth*, vol. 94, no. B7, pp. 9183–9191, 1989.

[2] E. J. Rignot and J. J. Van Zyl, "Change detection techniques for ers-1 sar data," *IEEE Transactions on Geoscience and Remote sensing*, vol. 31, no. 4, pp. 896–906, 1993.

[3] A. Ferretti, A. Monti-Guarnieri, C. Prati, F. Rocca, and D. Massonet, *InSAR principles-guidelines for SAR interferometry processing and interpretation*, 2007, vol. 19.

[4] S. Stramondo, F. R. Cinti, M. Dragoni, S. Salvi, S. Santini *et al.*, "The august 17, 1999 izmit, turkey, earthquake: Slip distribution from dislocation modeling of dinsar and surface offset," *Annals of Geophysics*, 2002.

[5] A. Refice, F. Bovenga, L. Guerriero, and J. Wasowski, "Dinsar applications to landslide studies," in *IGARSS 2001. Scanning the Present and Resolving the Future. Proceedings. IEEE 2001 International Geoscience and Remote Sensing Symposium (Cat. No. 01CH37217)*, vol. 1. IEEE, 2001, pp. 144–146.

Authorized licensed use limited to: Imperial College London. Downloaded on March 01,2024 at 10:36:50 UTC from IEEE Xplore. Restrictions apply.
© 2024 IEEE. Personal use is permitted, but republication/redistribution requires IEEE permission. See https://www.ieee.org/publications/rights/index.html for more information.

This article has been accepted for publication in IEEE Transactions on Geoscience and Remote Sensing. This is the author's version which has not been fully edited and content may change prior to final publication. Citation information: DOI 10.1109/TGRS.2024.3369509

[6] N. J. Schneevoigt, M. Sund, W. Bogren, A. Kääb, and D. J. Weydahl, "Glacier displacement on comfortlessbreen, svalbard, using 2-pass differential sar interferometry (dinsar) with a digital elevation model," *Polar record*, vol. 48, no. 1, pp. 17–25, 2012.

[7] H. A. Zebker, P. Rosen, S. Hensley, and P. J. Mouginis-Mark, "Analysis of active lava flows on kilauea volcano, hawaii, using sir-c radar correlation measurements," *Geology*, vol. 24, no. 6, pp. 495–498, 1996.

[8] H. R. Dietterich, M. P. Poland, D. A. Schmidt, K. V. Cashman, D. R. Sherrod, and A. T. Espinosa, "Tracking lava flow emplacement on the east rift zone of kīlauea, hawai 'i, with synthetic aperture radar coherence," *Geochemistry, Geophysics, Geosystems*, vol. 13, no. 5, 2012.

[9] T. Strozzi, A. Luckman, T. Murray, U. Wegmuller, and C. L. Werner, "Glacier motion estimation using sar offset-tracking procedures," *IEEE Transactions on Geoscience and Remote Sensing*, vol. 40, no. 11, pp. 2384–2391, 2002.

[10] A. Solgaard, A. Kusk, J. P. Merryman Boncori, J. Dall, K. D. Mankoff, A. P. Ahlstrøm, S. B. Andersen, M. Citterio, N. B. Karlsson, K. K. Kjeldsen *et al.*, "Greenland ice velocity maps from the promice project," *Earth System Science Data*, vol. 13, no. 7, pp. 3491–3512, 2021.

[11] C. Wang, X. Mao, and Q. Wang, "Landslide displacement monitoring by a fully polarimetric sar offset tracking method," *Remote Sensing*, vol. 8, no. 8, p. 624, 2016.

[12] A. M. A. Mahmoud, A. Novellino, E. Hussain, S. Marsh, P. Psimoulis, and M. Smith, "The use of sar offset tracking for detecting sand dune movement in sudan," *Remote Sensing*, vol. 12, no. 20, p. 3410, 2020.

[13] L. Bruzzone and D. F. Prieto, "An adaptive parcel-based technique for unsupervised change detection," *International Journal of Remote Sensing*, vol. 21, no. 4, pp. 817–822, 2000.

[14] R. G. Negri and A. C. Frery, "Unsupervised change detection driven by floating references: a pattern analysis approach," *Pattern Analysis and Applications*, vol. 24, no. 3, pp. 933–949, 2021.

[15] N. R. Gomes, M. I. Pettersson, V. T. Vu, P. Dammert, and H. Hellsten, "Likelihood ratio test for incoherent wavelength-resolution sar change detection," in *2016 CIE International Conference on Radar (RADAR)*. IEEE, 2016, pp. 1–4.

[16] L. Jia, M. Li, Y. Wu, P. Zhang, G. Liu, H. Chen, and L. An, "Sar image change detection based on iterative label-information composite kernel supervised by anisotropic texture," *IEEE Transactions on Geoscience and Remote Sensing*, vol. 53, no. 7, pp. 3960–3973, 2015.

[17] X. Hou, Y. Bai, Y. Xie, H. Ge, Y. Li, C. Shang, and Q. Shen, "Deep collaborative learning with class-rebalancing for semi-supervised change detection in sar images," *Knowledge-Based Systems*, vol. 264, p. 110281, 2023.

[18] L. Jia, M. Li, P. Zhang, and Y. Wu, "Sar image change detection based on correlation kernel and multistage extreme learning machine," *IEEE Transactions on Geoscience and Remote sensing*, vol. 54, no. 10, pp. 5993–6006, 2016.

[19] K. Conradsen, A. A. Nielsen, J. Schou, and H. Skriver, "Change detection in polarimetric sar data and the complex wishart distribution," in *IGARSS 2001. Scanning the Present and Resolving the Future. Proceedings. IEEE 2001 International Geoscience and Remote Sensing Symposium (Cat. No. 01CH37217)*, vol. 6. IEEE, 2001, pp. 2628–2630.

[20] ——, "A test statistic in the complex wishart distribution and its application to change detection in polarimetric sar data," *IEEE Transactions on Geoscience and Remote Sensing*, vol. 41, no. 1, pp. 4–19, 2003.

[21] A. D. Nascimento, A. C. Frery, and R. J. Cintra, "Detecting changes in fully polarimetric sar imagery with statistical information theory," *IEEE Transactions on Geoscience and Remote Sensing*, vol. 57, no. 3, pp. 1380–1392, 2018.

[22] R. G. Negri and A. C. Frery, "A general and extensible framework for assessing change detection techniques," *Computers & Geosciences*, vol. 178, p. 105390, 2023.

[23] A. M. Atto, F. Bovolo, and L. Bruzzone, *Change Detection and Image Time Series Analysis 2: Supervised Methods*. John Wiley & Sons, 2021.

[24] ——, *Change detection and image time-series analysis. 1 : unsupervised methods*, 1st ed. Hoboken, NJ: John Wiley & Sons, Inc., 2022.

[25] J. W. Goodman, "Statistical properties of laser speckle patterns," in *Laser speckle and related phenomena*. Springer, 1975, pp. 9–75.

[26] J. Jao, "Amplitude distribution of composite terrain radar clutter and the κ-distribution," *IEEE Transactions on Antennas and Propagation*, vol. 32, no. 10, pp. 1049–1062, 1984.

[27] A. C. Frery, H.-J. Muller, C. d. C. F. Yanasse, and S. J. S. Sant'Anna, "A model for extremely heterogeneous clutter," *IEEE transactions on geoscience and remote sensing*, vol. 35, no. 3, pp. 648–659, 1997.

[28] H.-C. Li, W. Hong, Y.-R. Wu, and P.-Z. Fan, "On the empirical-statistical modeling of sar images with generalized gamma distribution," *IEEE Journal of selected topics in signal processing*, vol. 5, no. 3, pp. 386–397, 2011.

[29] M. E. Mejail, J. C. Jacobo-Berlles, A. C. Frery, and O. H. Bustos, "Classification of sar images using a general and tractable multiplicative model," *International Journal of Remote Sensing*, vol. 24, no. 18, pp. 3565–3582, 2003.

[30] J. Gambini, M. E. Mejail, J. Jacobo-Berlles, and A. C. Frery, "Accuracy of edge detection methods with local information in speckled imagery," *Statistics and Computing*, vol. 18, pp. 15–26, 2008.

[31] W. MingChun, Z. JiaFeng, and L. Tao, "Constant false alarm rate detection method in polarimetric synthetic aperture radar imagery based on whitening filter under inverse beta distribution," *The Journal of Engineering*, vol. 2019, no. 19, pp. 5574–5579, 2019.

[32] R. Saunders, G. Pettengill, R. Arvidson, W. Sjogren, W. Johnson, and L. Pieri, "The magellan venus radar mapping mission," *Journal of Geophysical Research: Solid Earth*, vol. 95, no. B6, pp. 8339–8355, 1990.

[33] T. Widemann, R. Ghail, C. F. Wilson, and D. V. Titov, "Envision: Europe's proposed mission to venus," in *Agu fall meeting abstracts*, vol. 2020, 2020, pp. P022–02.

[34] S. Smrekar, S. Hensley, R. Nybakken, M. S. Wallace, D. Perkovic-Martin, T.-H. You, D. Nunes, J. Brophy, T. Ely, E. Burt *et al.*, "Veritas (venus emissivity, radio science, insar, topography, and spectroscopy): a discovery mission," in *2022 IEEE Aerospace Conference (AERO)*. IEEE, 2022, pp. 1–20.

[35] R. D. Lorenz, "Probabilistic constraints from existing and future radar imaging on volcanic activity on venus," *Planetary and Space Science*, vol. 117, pp. 356–361, 2015.

[36] P. K. Byrne and S. Krishnamoorthy, "Estimates on the frequency of volcanic eruptions on venus," *Journal of Geophysical Research: Planets*, vol. 127, no. 1, p. e2021JE007040, 2022.

[37] T. Widemann, S. E. Smrekar, J. B. Garvin, A. G. Straume-Lindner, A. C. Ocampo, M. D. Schulte, T. Voirin, S. Hensley, M. D. Dyar, J. L. Whitten *et al.*, "Venus evolution through time: key science questions, selected mission concepts and future investigations," *Space Science Reviews*, vol. 219, no. 7, p. 56, 2023.

[38] S. Hensley, B. Campbell, D. Perkovic-Martin, K. Wheeler, W. Kiefer, and R. Ghail, "Visar and vensar: Two proposed radar investigations of venus," in *2020 IEEE Radar Conference (RadarConf20)*. IEEE, 2020, pp. 1–6.

[39] C. Oliver and S. Quegan, *Understanding synthetic aperture radar images*. SciTech Publishing, 2004.

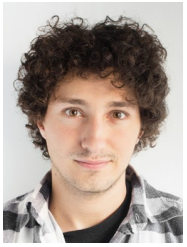
[40] J. Durand, B. Gimonet, and J. Perbos, "Speckle in sar images: An evaluation of filtering techniques," *Advances in Space Research*, vol. 7, no. 11, pp. 301–304, 1987.

[41] R. Touzi, A. Lopes, and P. Bousquet, "A statistical and geometrical edge detector for sar images," *IEEE Transactions on geoscience and remote sensing*, vol. 26, no. 6, pp. 764–773, 1988.

Authorized licensed use limited to: Imperial College London. Downloaded on March 01,2024 at 10:36:50 UTC from IEEE Xplore. Restrictions apply.
© 2024 IEEE. Personal use is permitted, but republication/redistribution requires IEEE permission. See https://www.ieee.org/publications/rights/index.html for more information.

This article has been accepted for publication in IEEE Transactions on Geoscience and Remote Sensing. This is the author's version which has not been fully edited and content may change prior to final publication. Citation information: DOI 10.1109/TGRS.2024.3369509

[42] N. Otsu, "A threshold selection method from gray-level histograms," *IEEE transactions on systems, man, and cybernetics*, vol. 9, no. 1, pp. 62–66, 1979.
[43] R. N. Bradt, "E. s. keeping, introduction to statistical inference (d. van nostrand co., princeton, n.j., 1962), xi 451 pp., 66s." *Proceedings of the Edinburgh Mathematical Society*, vol. 13, no. 3, p. 264–264, 1963.
[44] J. B. McDonald, "Some generalized functions for the size distribution of income," *Modeling income distributions and Lorenz curves*, pp. 37–55, 2008.
[45] B. A. Campbell, *Use and presentation of Magellan quantitative data in Venus mapping*. US Department of the Interior, US Geological Survey, 1995.
[46] K. S. Rao and V. Lakshminarayanan, *Generalized Hypergeometric Functions: transformations and group theoretical aspects*. IOP Publishing, 2018.
[47] H. Bateman, *Higher transcendental functions [volumes i-iii]*. McGRAW-HILL book company, 1953, vol. 1.
[48] G. Casella and R. L. Berger, *Statistical inference*. Cengage Learning, 2021.
[49] Washington University in St. Louis / NASA, "About PDS: Long-term archive of digital data products returned from nasa's planetary missions," n.d., accessed since March 1, 2022. https://pds-geosciences.wustl.edu/.
[50] D. O. Muhleman, "Radar scattering from venus and mercury at 12.5 cm," *Radio Sci. D*, vol. 69, pp. 1630–1631, 1965.
[51] G. H. Pettengill, P. G. Ford, W. T. Johnson, R. K. Raney, and L. A. Soderblom, "Magellan: Radar performance and data products," *Science*, vol. 252, no. 5003, pp. 260–265, 1991.



Gerard Gallardo i Peres was born in Barcelona in 1997. He received a B.Sc. degree in Aerospace Engineering from the Universitat Politècnica de Catalunya in 2019, following his thesis work on CubeSat power system design at Politecnico di Milano. He later received a M.Sc. degree in Earth and Space Physics and Engineering from the Technical University of Denmark, specializing in Space Research by means of Synthetic Aperture Radar. Since 2019 he has been working with isardSAT S.L. in Earth Observation satellite projects, including CryoSAT-1 and Sentinel-6. He is currently a PhD student at the Royal School of Mines, Imperial College London, and his research focuses on the simulation of future SAR imagery on Venus and its applications for change detection and geomorphology.



Jørgen Dall (Member, IEEE) received the M.Sc. degree in electrical engineering and the Ph.D. degree from the Technical University of Denmark in 1984 and 1989, respectively. He is a professor in microwave remote sensing systems at the Technical University of Denmark. He has contributed to the development of the Danish airborne SAR, EMISAR, notably he led the development of a dedicated real-time SAR processor, was responsible for the offline data processing, and organized the EMISAR data acquisition campaigns in a five-year period. Later, he led the development of ESA's airborne SAR and Ice Sounding radar, POLARIS. Most recently he led the development of an experimental X-band MIMO radar. His research interests include various aspects of ice sheet mapping using InSAR, PolInSAR and TomoSAR techniques as well as radar ice sounding.



Philippa J Mason received a BSc in Geology from Southampton University in 1987, an MSc in Remote Sensing from University College London in 1993, and PhD from Imperial College London in 1999. She is currently Senior Lecturer in the Department of Earth Science & Engineering at Imperial College London. Her teaching activities include UG and MSc courses in remote sensing and image processing, and supervision of MSc and PhD students. Her research is focused on Earth and planetary remote sensing applications: development of time-series InSAR and other tools using Earth Observation data across geoscience and environmental challenges; and in development of new tools for geological change detection and geomorphological mapping of radar imagery on Venus. She is a member of both the Science Study Team and the VenSAR Science Team for the forthcoming ESA/NASA EnVision mission to Venus.



Richard Ghail is a professor in engineering geology and planetary science at Royal Holloway, University of London. He specialises in the use radar interferometry (InSAR) to measure ground movements at the millimetre per year level, and leads the MSc in Engineering Geology and Hydrogeology. Previously at Imperial College London he founded the Engineering Scale Geology Research Group to study and develop radar-based ground investigation techniques, and led EnVision, the European Space Agency's mission to Venus, which will use radar to characterise and measure tectonic activity on Venus. He obtained a BSc in Geology from Imperial College and a PhD researching tectonics on Venus from Lancaster University.



Scott Hensley received his BS degrees in Mathematics and Physics from the University of California at Irvine and the Ph.D. in Mathematics from Stony Brook University where he specialized in the study of differential geometry. In 1991, Dr. Hensley joined the staff of the Jet Propulsion Laboratory where he is currently a Senior Research Scientist studying advanced radar techniques for geophysical applications. He has worked on the Magellan and Cassini radars, was the GeoSAR Chief Scientist, lead the SRTM Interferometric Processor Development Team, and was Principal Investigator and is currently the Project Scientist for the NASA UAVSAR program. He is also the project Scientist for the recently selected VERITAS and EnVision missions to Venus. He is an IEEE Fellow.

Authorized licensed use limited to: Imperial College London. Downloaded on March 01,2024 at 10:36:50 UTC from IEEE Xplore. Restrictions apply.
© 2024 IEEE. Personal use is permitted, but republication/redistribution requires IEEE permission. See https://www.ieee.org/publications/rights/index.html for more information.